applied sciences

MDPI

Article

Study of Annealing Temperature Effect on the Photovoltaic Performance of BiOI-Based Materials

Anissa A. Putri [1,2], Shinya Kato [1], Naoki Kishi [1] and Tetsuo Soga [1,*]

[1] Department of Electrical and Mechanical Engineering, Nagoya Institute of Technology, Nagoya 466-8555, Japan
[2] Department of Chemistry, Walisongo State Islamic University, Semarang 50185, Indonesia
* Correspondence: soga@nitech.ac.jp; Tel.: +81-52-735-5532

Received: 2 August 2019; Accepted: 10 August 2019; Published: 14 August 2019

Abstract: Bismuth oxyiodide (BiOI) is expected to be promising material for photovoltaic devices since it has good activity under the visible range. Here, we studied the annealing treatment on BiOI and its effect on the photovoltaic application. Firstly, the synthesized BiOI from $Bi(NO_3)_3$ and KI was annealed at varied temperatures (100–550 °C). The structural investigation by X-ray diffraction and Raman spectroscopy analysis was supported with morphology and optical analysis by scanning electron microscope (SEM) and UV-Visible spectroscopy. Due to the heating treatment, it could result in iodine-deficient bismuth-based materials, namely $Bi_7O_9I_3$, Bi_5O_7I, and β-Bi_2O_3. Secondly, the photovoltaic test measurement was performed by solar simulator air mass (AM) 1.5 illumination which presented the current-voltage curve from each material. The enhancement of photovoltaic performance was given by the increase of temperature up to 300 °C. At that temperature, the performance of the device which consisted of $Bi_7O_9I_3$ achieved three times higher efficiency than the annealed parent BiOI at 100 °C. Hence, the structural changing owing to the oxygen addition to BiOI structure had an impact on the photoelectrochemical cell. Based on this work, it is possible to attempt BiOI derivation with suitable holes and electron transport layers for better photovoltaic performance.

Keywords: BiOI; annealing; iodine-deficient; photovoltaic

1. Introduction

Bismuth oxyiodide (BiOI) is a p-type semiconductor which is commonly applied as a photocatalyst for photocatalytic reaction during the last decade [1–9]. Since it has the bandgap energy ~1.8 eV, this material has good absorption in the visible spectral range. It is interesting to note that this oxyhalide semiconductor also has an environmentally benign character [10]. The wider application of BiOI can extend for a photoanode used in photoelectrochemical devices [11–17]. Several ways are common to synthesize BiOI, either including the solvent usage or solvent-less process [5,11,16,18–20]. Generally, hydrothermal and solvothermal methods are used to produce BiOI powder for photocatalytic application [9,18,19]. However, successive ionic layer adsorption and reaction, as well as chemical-based deposition have been employed to deposit BiOI films for photovoltaic study [13,14,16]. Nevertheless, as an alternative, the BiOI film's preparation for solar cell application also can be carried out via the doctor blade method which will be discussed in this report.

Some key aspects of semiconductor materials' properties are noted to be a crucial matter for the device performance as different parameters in synthesis can result in different physical properties of materials. The morphology, size, crystallinity, and optical properties are needed to be considered, since those characteristics can be affected by the procedure of materials preparation, the concentration of precursors [21–23], surfactant selection, and solvent selection [24,25]. The post-treatment after the

material synthesis process, like calcination, also can change the material properties. It seems to be similar to the BiOI structure, since it consists of $[Bi_2O_2]^{2+}$ slabs that allow for stoichiometric changing due to the calcination for producing the derivate of BiOI [26]. Moreover, the pH adjustment during the synthesis process is an important factor which affects BiOI structure [1].

BiOI and its derivation have been reported mostly for photocatalytic application due to their effectivity in the separation of electron-hole pairs [27]. $Bi_4O_5I_2$, with its smaller size and wider valence band, had a better photocatalytic performance than BiOI because it had a lower electron-hole pairs recombination rate [28]. $Bi_7O_9I_3$, which is often difficult to differ with BiOI, was also reported to have excellent photocatalytic activity under visible light irradiation [26,29]. Another BiOI family member is Bi_5O_7I, which exhibited a twice higher photocatalytic activity than BiOI because of its pores and different band structure [30]. Moreover, polymorphic Bi_2O_3 could show its ability as photocatalyst with performance order: $\beta - Bi_2O_3 > \alpha - Bi_2O_3 > \delta - Bi_2O_3$ [31], but it has not been compared yet with BiOI activity. Many reports on BiOI and its derivatives for photocatalytic application have been reported. However, to the best our knowledge, there is no study in the screening of BiOI and its derivations for photovoltaic device application, even though BiOI can be considered as the promising material for the future photovoltaic devices owing to its longer lifetime which up to 2.7 ns [11].

In this study, we investigated the effect of annealing treatment in air at different temperatures on the structural, morphological, optical, and photovoltaic properties of BiOI films. By changing the temperature from 100 °C to 550 °C, we could obtain different characteristics of bismuth-based material, both chemically and physically. The heating process in the air let the reaction occur by turning into the oxygen-rich materials as a consequence of losing some iodine in the parent BiOI structure. Through the photoelectrochemical cell performance evaluation, which was constructed by BiOI with I^-/I_3^- electrolyte and Pt/Fluorine-doped tin oxide glass (Pt-FTO) as a counter electrode, we obtained the best performance from $Bi_7O_9I_3$ as the annealed BiOI films at 300 °C. Based on this result, we expect that this study can open future work in photovoltaic application based on the BiOI. $Bi_7O_9I_3$ may show the greater photovoltaic performance by utilizing a different structure with appropriate hole and electron transport materials inside.

2. Materials and Methods

2.1. Synthesis of BiOI and Its Derivation

During the experiment, we used $Bi(NO_3)_3{\cdot}5H_2O$ as a cation source and KI as an anion source (Nacalai Tesque, Inc. Kyoto, Japan). The ultrapure water from Milli-Q direct water purification system with resistivity (18.2 MΩ-cm at 25 °C) was used as the solvent. All of the chemicals were utilized without any further treatment and purification.

Here, we reported the BiOI preparation through 15 min direct grinding of 2 mmol $Bi(NO_3)_3{\cdot}5H_2O$ and KI as solid precursors. This step was followed by a hydrolysis reaction of precursors via 40 mL deionized water addition, and the black paste from the mixed-precursor turned to the orange mixture due to the hydrolysis. Next, the as-BiOI was stirred for 5 h at room temperature to obtain BiOI powder. Eventually, BiOI powder was rinsed with ethanol and deionized water for several times.

To get BiOI paste, the collected precipitated BiOI was mixed with ethanol for a 5 min dispersion process by a homogenizer. Subsequently, the paste was deposited onto a cleaned FTO glass substrate via the doctor blade method. Finally, the deposited BiOI on FTO substrates were treated by the heating process at a different temperature, i.e., 100 °C, 200 °C, 300 °C, 450 °C, and 550 °C for 1 h. The film thickness measurement was carried out using alpha-step 500, and the average measured thickness of each film was around 1.5 μm.

2.2. Characterization and Photovoltaic Cell Fabrication

Characterization was carried out for the samples by X-ray diffraction (Rigaku RINT-2100 diffractometer), Raman spectrometry (JASCO NRS-2100), FESEM (JEOL JSM-7100F), and UV Visible

spectroscopy (JASCO 670 UV). We applied all of the samples as the photoanode component in our photovoltaic devices to study their performances due to the heating treatment. The cell structure was FTO/BiOI/Iodine electrolyte/Pt-FTO. The active area for light illumination was designed with the dimension 0.16 cm^2. To measure the cell performance, we used solar simulator (100 mW/cm^2; AM 1.5 illumination which is categorized as laboratory class solar simulator using a Xenon lamp/ Class AAA spectra).

3. Results and Discussion

3.1. Structure Analysis

3.1.1. X-Ray Diffraction

Figure 1 shows the XRD patterns of BiOI and its family members as a result of the heating treatment. The different XRD patterns in the annealed BiOI films can be observed in Figure 1. The treatment at 100 °C displayed the existing BiOI crystal plane, which was matched to the Joint Committee on Powder Diffraction Standards (JCPDS) card of BiOI No. 00-73-2062. The crystal planes (001), (002), (102), (110), (013), (004), (200), (114), and (122) appeared at 2θ around 9.6°, 19.3°, 29.8°, 31.86°, 36.8°, 39.2°, 45.8°, 51.2°, and 55°, respectively. The similar pattern of annealed BiOI at 200 °C and 300 °C to the treated sample at 100 °C was also noticeable. An identical pattern was only observed in the heated BiOI at 100 °C and 200 °C with the different intensities of both materials. However, a slight decrease in the 2θ shift was detected from the annealed BiOI at 300 °C in comparison to those treated samples at 100 °C and 200 °C, whereas (102), (110), and (200) crystal planes were in 29.7°, 31.8°, and 45.7°. In spite of its pattern being the same as the BiOI crystallinity at the lower temperature without any impurity peaks, we supposed that the distortion in BiOI crystal structure might happen during the heating treatment at 300 °C. Hence, it resulted in the smaller 2θ compared with those of BiOI diffractograms. The expansion and distortion of BiOI structure can be attributed by the more bismuth and oxygen contained in the BiOI lattice crystal [29]. Regarding this phenomenon, we expected that the chemical structure of the annealed sample at 300 °C transformed to the different structure ($Bi_7O_9I_3$), since a heating treatment allowed for the oxygen and iodine addition and subtraction. Some researchers claimed that it is difficult to distinguish BiOI and $Bi_7O_9I_3$ because both materials have similar XRD pattern [26]. We also believe that the annealed material at 300 °C was not $Bi_4O_5I_2$ since between $Bi_7O_9I_3$ and $Bi_4O_5I_2$ show the different pattern by XRD [28]. Additionally, the similar binding energy in the Bi and I region of BiOI and $Bi_7O_9I_3$ [32] made those materials difficult to differentiate by their X-ray photoelectron spectroscopy (XPS) spectra. To clarify, we found a different (110) d-spacing value in both materials, which indicated that the annealed material at 300 °C was dissimilar to the treated material at 100 °C. Both 0.285 and 0.280 nm d-spacing were obtained for the treated material at 300 °C and 100 °C, respectively. The d-spacing value of our BiOI was matched to the reported work by Ren and co-workers [33], and the value for d-spacing of the treated sample at 300 °C was near from the Transmission Electron Microscopy (TEM) d-spacing material for $Bi_7O_9I_3$ (0.286 nm) [34]. Therefore, we propose that our annealed material at 300 °C was $Bi_7O_9I_3$, and it is important to note that the bigger d-spacing may be affected by the aforementioned distortion in BiOI standard structure.

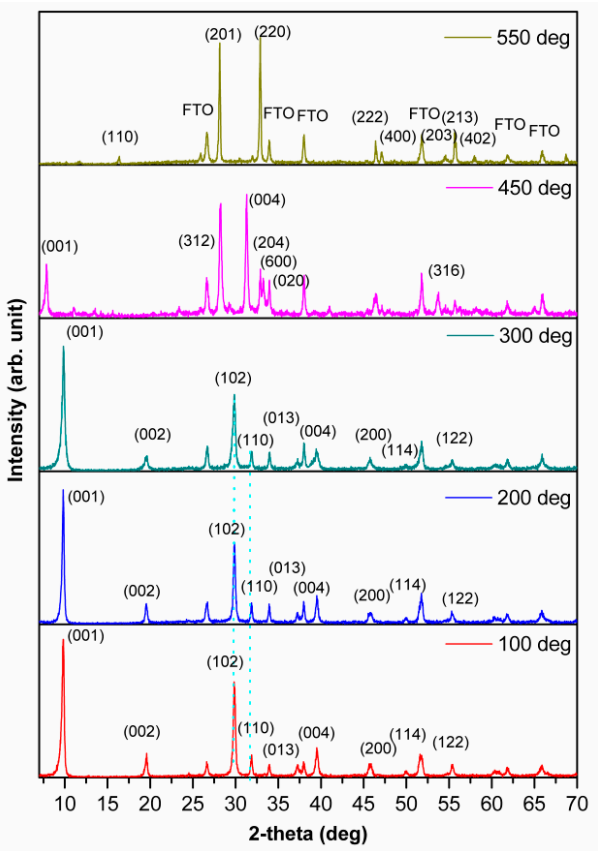

Figure 1. XRD pattern of annealed BiOI at varied temperatures: 100 °C, 200 °C, 300 °C, 450 °C, and 550 °C.

To study more about the quantitative aspect of BiOI crystal, the average crystal size value of annealed BiOI at 100 °C, 200 °C, and 300 °C was calculated using the Debye–Scherrer equation, $L = K\lambda/\beta Cos\theta$, in which L represents the crystallite size, K (0.9) is the constant, λ (0.154 nm) is the wavelength of Cu, β is the FWHM (full width at half maximum; in radian), and θ is the Bragg angle. We obtained the average values of crystallite size around 29.97 nm, 33.06 nm, and 27.42 nm for annealed materials at 100 °C, 200 °C, and 300 °C. Based on these results, it is noted that the heating process had an impact on crystal size distribution [35]. Normally, an increase in annealing temperature causes an increase in a grain size since a higher annealing temperature leads to crystal growth by producing the larger crystallites number. Hence, the crystal size increases as the consequence of the lesser crystal defect in the higher temperature condition. However, we observed that the smaller crystal size was acquired in the annealed material at 300 °C than in the annealed BiOI at 100 °C and 200 °C. These data are supported by the broadening FWHM peak of annealed BiOI at 300 °C, as is shown in Figure 1. We assume that the broader peak reflects the less number of BiOI crystallites owing to the BiOI transformation to bismuth and oxygen-rich material, like $Bi_7O_9I_3$. Based on the Debye–Scherrer equation, we noted that the broader peak related to the declining in the crystal size value.

The XRD patterns of the annealed BiOI at 450 °C and 550 °C reveal the crystal character of Bi_5O_7I and β-Bi_2O_3 crystals. Referring to the JCPDS card No. 00-40-0548, it was found that Bi_5O_7I crystal planes were assigned to the (001), (312), (004), (204), (020), and (316) at 2θ around 7.7°, 28.2°, 31.09°, 33.02°, 33.4°, and 53.6°. Moreover, Figure 1 shows the crystal plane (201) and (220) at 2θ were around 27.9° and 32.6°, which correspond to the tetragonal β-Bi_2O_3 for the annealed sample at 550 °C. This is matched to the data in the JCPDS card No. 00-27-0050 and previous research [36]. Our Bi_5O_7I pattern is

in line with the reported research [37]. Overall, the heating treatment on BiOI changes its composition and structures, as is illustrated in the proposed reaction:

$$7BiOI + O_2 \rightarrow Bi_7O_9I_3 + 2I_2 \quad (1)$$

$$5Bi_7O_9I_3 + 2O_2 \rightarrow 7Bi_5O_7I + 4I_2 \quad (2)$$

$$4Bi_5O_7I + O_2 \rightarrow 10Bi_2O_3 + 2I_2 \quad (3)$$

3.1.2. Raman Spectroscopy

Another structural study in annealing effect of BiOI materials was also investigated by Raman spectroscopy analysis. The results of the Raman analysis are shown in Figure 2. It has been confirmed in many reports that BiOI has Bi-I characteristic in Raman spectra which can be identified by its vibration mode at 147–149 cm^{-1} [38,39]. This information was also obtained in the annealed BiOI at 100 °C and 300 °C. Similar to the XRD analysis results (Figure 1), the Raman spectra of annealed BiOI in those temperatures had a nearly identical pattern without the marked impurity peak from other bismuth-based materials.

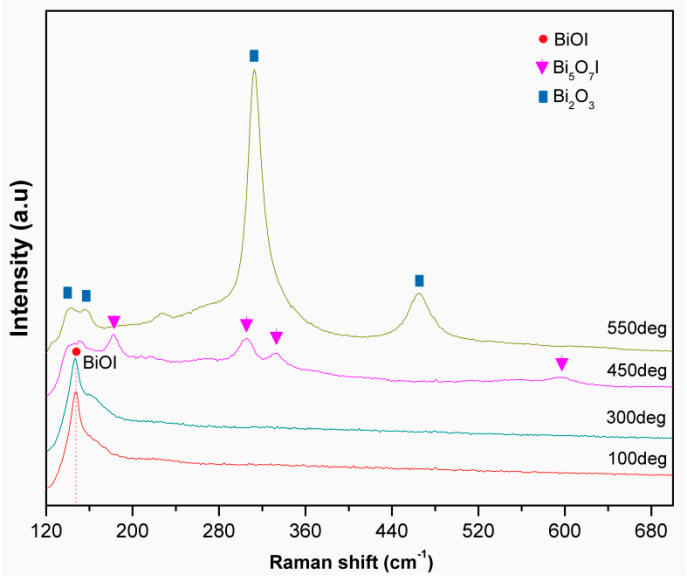

Figure 2. Raman spectra of annealed BiOI at different temperatures: 100 °C, 300 °C, 450 °C, and 550 °C.

After the samples were heated at a higher temperature, the vibration mode of Bi–I shifted to the higher frequency. It is shown like in the Raman spectra of $Bi_4O_5I_2$ and Bi_5O_7I. It was also same as the reported work by Liu and co-workers [40]. The annealing treatment of BiOI at 550 °C can result in a different trend in its Raman spectra, as it can result in a change of BiOI chemical structure. We found the peak signals around 280–350 cm^{-1} and 445–485 cm^{-1}, which are close to the characteristic of β-Bi_2O_3 [41]. By observing the XRD patterns and Raman spectra in Figures 1 and 2, we note that among the structure of BiOI and its derivations, Bi_5O_7I and Bi_2O_3 are different from others.

The aforementioned reactions in Equations (1)–(3) were considered as thermal decomposition reactions, whereas the deiodination reaction results in new materials. During the reaction, the gasifying and evaporation of I_2 happened due to the heating treatment of BiOI to bring out the derivation of oxygen-rich and iodine-deficient bismuth oxyhalides materials [30].

3.2. Morphology Analysis

The SEM images of some annealed BiOI are depicted in Figure 3. From Figure 3A,B, it is obvious that there was no significant difference in the shape of annealed BiOI at 100 °C and 300 °C. Both samples

had irregular nanosheet forms with smooth surfaces. However, we observed that there were some smaller sheets in the annealed BiOI at 100 °C and 300 °C. The growth direction of the irregular BiOI sheet in this report was dominated by the (001) facet growth. This was in line with its XRD patterns. This circumstance might be affected by the amount of water added in the hydrolysis reaction during BiOI synthesis. If the more water was introduced to $Bi(NO_3)_3$ in the early step of the reaction, the hydrolysis and nucleation rate were faster due to the less concentration of $Bi(NO_3)_3$ and the weaker acidic solution. As a result, the BiOI layer growth along the (110) was dominant. In contrast, due to the less amount of water put into the precursor solution, it induced the BiOI (001) facet growth; this is in line with reported research [2,42]. The measured layer thickness of BiOI nanosheets was around 37.5 nm and 25 nm (Figure 3E,F) for annealed BiOI at 100 °C and 300 °C, respectively.

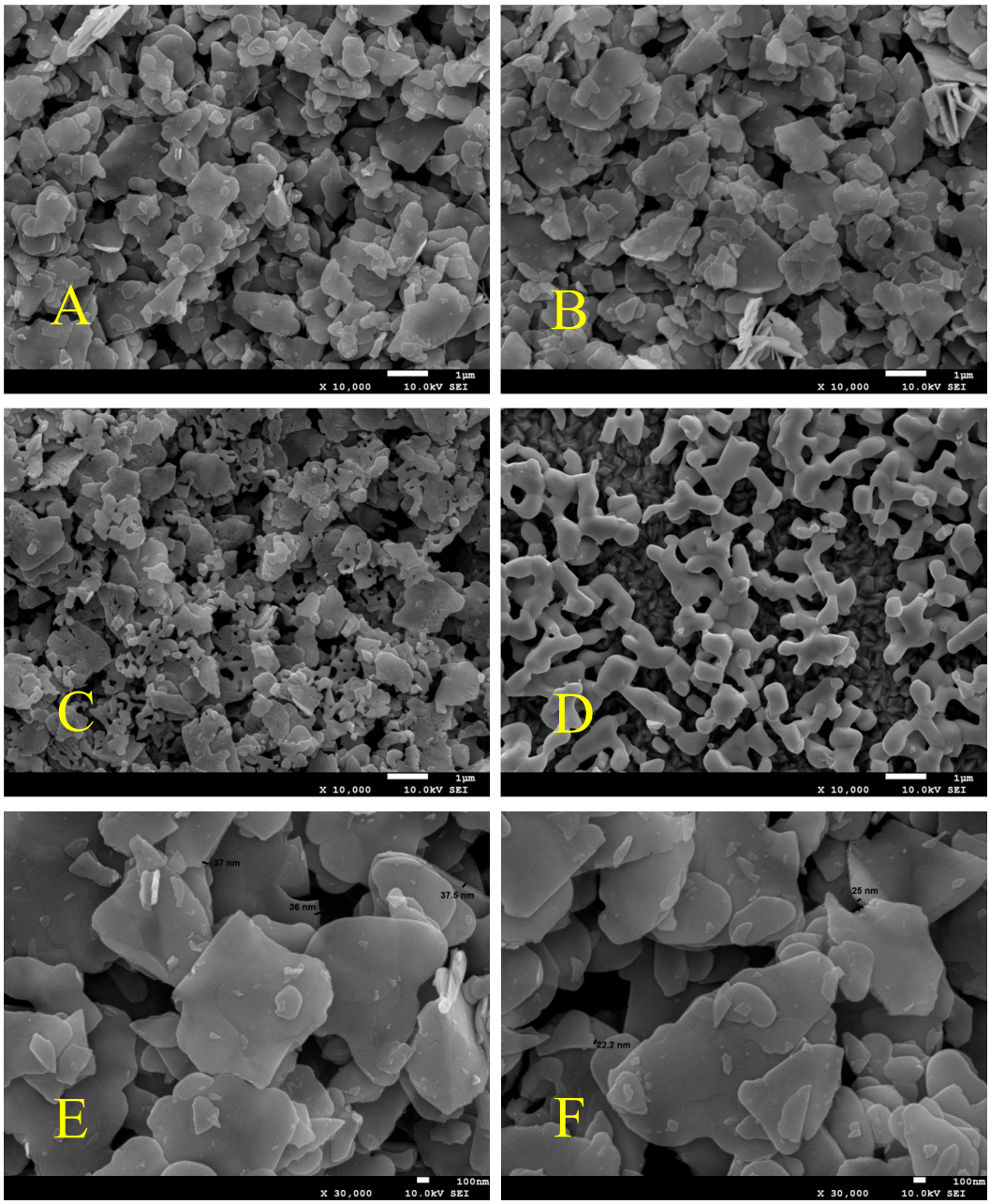

Figure 3. SEM images of annealed BiOI at different temperatures: 100 °C, 300 °C, 450 °C, 550 °C (**A**–**D**); and the higher magnification image of the annealed sample at 100 °C and 300 °C (**E**,**F**).

For the annealed sample at 450 °C in Figure 3C, it can be seen that this material was also composed by nanosheets which were irregular, similar to the displayed images in Figure 3A,B. However, some pores appeared in the sample surface, and the width of sheets in Figure 3C tended to be smaller, with a sheet thickness of around 60 nm. This image is comparable with the synthesized Bi_5O_7I by Yang and co-workers [30]. Apart from Bi_5O_7I, the annealed sample at a higher temperature (550 °C) resulted in the biggest bismuth-based material like a dumbbell, with a thickness around 75 nm. The same morphology of this dumbbell-like material was also confirmed in the previous report for β-Bi_2O_3 [36]. Worm-like structures which are similar to our β-Bi_2O_3 morphology were also reported [31]. Due to the annealing treatment, the material transformation can relate to the shrinkage process, which results in more ordered phase as the effect of the less crystal defects. The shrinkage in our materials might have been caused by iodine deficiency and oxygen incorporation during the annealing process, like in the copper nitride material [43].

3.3. Optical Study

To obtain the optical property information, we used UV-Visible spectroscopy for its analysis. The absorbance spectra are displayed in Figure 4A. The absorbance value of each sample was determined from transmittance (T) and reflectance (R) values as the equation: $A = 1 - (T + R)$ [44]. The spectra in Figure 4A show that all of annealed BiOI from 100 °C to 550 °C had absorption in the visible range. However, the annealing treatment provoked the blue-shift in its absorption along with the increase in temperature. From Figure 4A, we can see that the absorption edge of annealed BiOI at 100 °C and 200 °C overlapped at a wavelength of more than 600 nm. Due to this same absorption trend, we predict that the material composition of those treated samples may have been the same. When the annealing treatment was increased up to 300 °C and more, the absorption edge of those materials tended to be lower. The maximum absorption of each material was near 600 nm, and it was below 600 nm for annealed materials at 450 °C and 550 °C. Therefore, this supports the prediction that the material structure in the annealed BiOI at 100 °C, 200 °C, 300 °C, 450 °C, and 550 °C could be BiOI, BiOI, $Bi_7O_9I_3$, Bi_5O_7I, and Bi_2O_3. The oxidation reaction due to the treatment to BiOI at a high temperature allowed the BiOI to transform into the different materials, which have lower absorption abilities of visible light relative to the parent material [30].

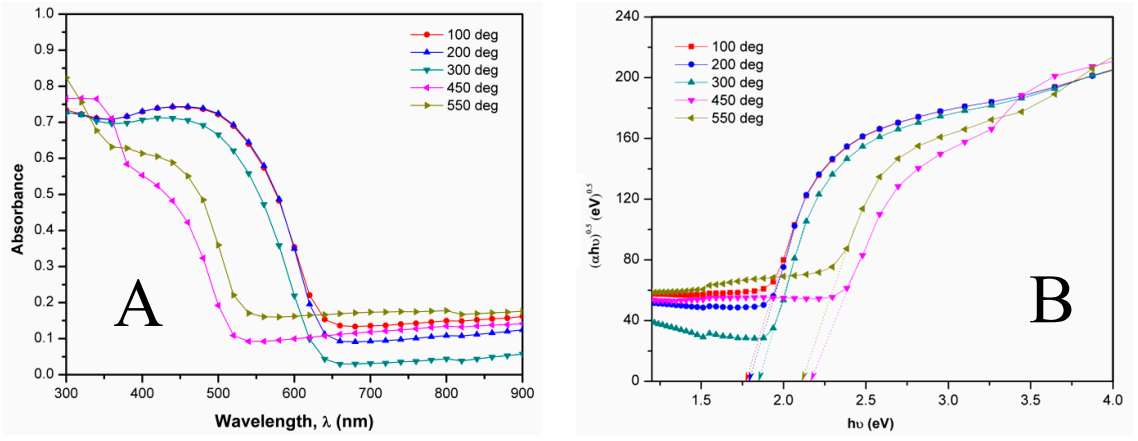

Figure 4. Absorbance spectra (**A**) and Tauc plot (**B**) of annealed BiOI at different temperatures.

All those materials can be classified as semiconductor materials. The bandgap energy of bismuth-based materials is commonly determined by the Tauc plot, $\alpha hv = A(hv - Eg)^{n/2}$, whereas α, h, v, Eg, n are the absorption coefficient, Planck constant, the frequency of photonic, bandgap energy, and the value which depends on the semiconductor interband transition. If $n = 4$, the material can be categorized to have the direct bandgap transition, while the indirect bandgap is categorized if $n = 1$ [9]. Since the indirect type belongs to the bandgap calculation for the BiOI family [30], the n value of

4 was taken for this bandgap determination in our materials. The indirect bandgap calculation for annealed BiOI is shown in Figure 4B. The calculated bandgap energy of annealed BiOI at 100 °C, 200 °C, 300 °C, 450 °C, and 550 °C as BiOI, BiOI, $Bi_7O_9I_3$, Bi_5O_7I, and Bi_2O_3 were 1.76, 1.77, 1.84, 2.18, and 2.11, respectively. The bandgap energy order haf a good agreement with the blue-shift phenomenon in the absorbance spectra of those annealed samples. Our bandgap energy of BiOI was also in line with the calculated BiOI from the previous report with order: $BiOI < Bi_7O_9I_3 < Bi_5O_7I$ which have the agreement with some references [26,45]. The bandgap energy of Bi_5O_7I was also reported to be slightly higher than Bi_2O_3 [46], and for β-Bi_2O_3, it was around 2.15 eV [47]. The structure changing in BiOI due to the annealing treatment influenced the bandgap energy as an effect of the different electronic structure in bismuth materials. The oxygen-deficient in the BiOI structure had a redshift response in the visible spectral range [48]. Thus, BiOI with oxygen-rich and iodine-deficient like in our materials had a blue shifting effect in their absorbance spectra.

3.4. Photovoltaic Test

We prepared the photovoltaic cells contained BiOI and its family members, as is illustrated in Figure 5A. The resulted current-voltage test of annealed BiOI in varied temperatures is displayed in Figure 6A and Table 1. Additionally, the dependence of short-circuit current (J_{sc}) and open-circuit voltage (V_{oc}) trend on the temperature is shown in Figure 6B. From Figure 6B, it can be seen that the increase in the temperature up to 300 °C resulted in the increasing of J_{sc} and V_{oc}. Then, it was followed by a reduction in cell performance due to the treatment for more than 450 °C. In our work, we made two devices for photovoltaic cell measurement, and, here, we show better data in Figure 6A from two devices to represent the J_{sc} and V_{oc} trend, which is displayed in Figure 6B. The wider light absorption could have been responsible for the higher J_{sc} value, as this factor can affect the light-harvesting ability of semiconductor materials due to the redshift effect [49]. Other factors which may have an impact on the J_{sc} are grain size, internal resistance, film quality, charge transfer model, and electron mobility.

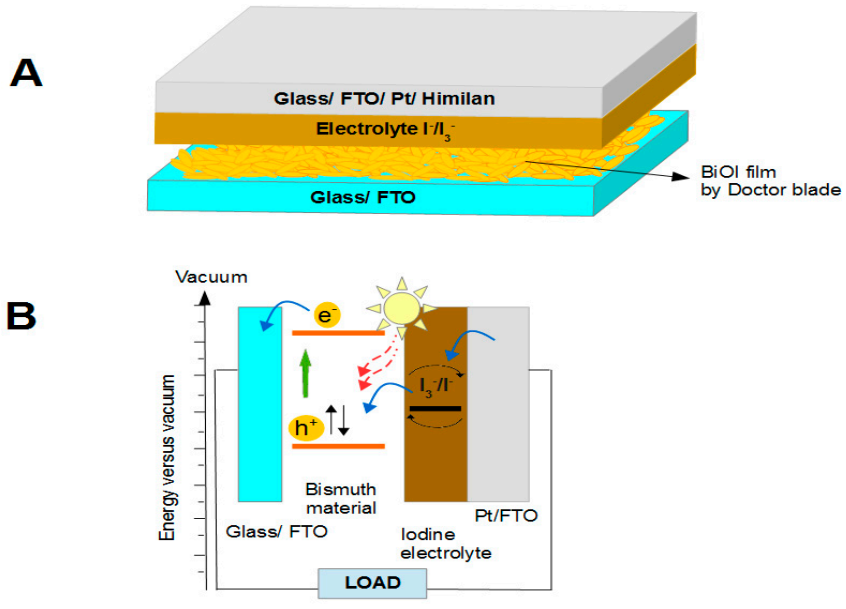

Figure 5. Device structure (**A**) and band structure illustration of annealed BiOI in different temperatures (**B**).

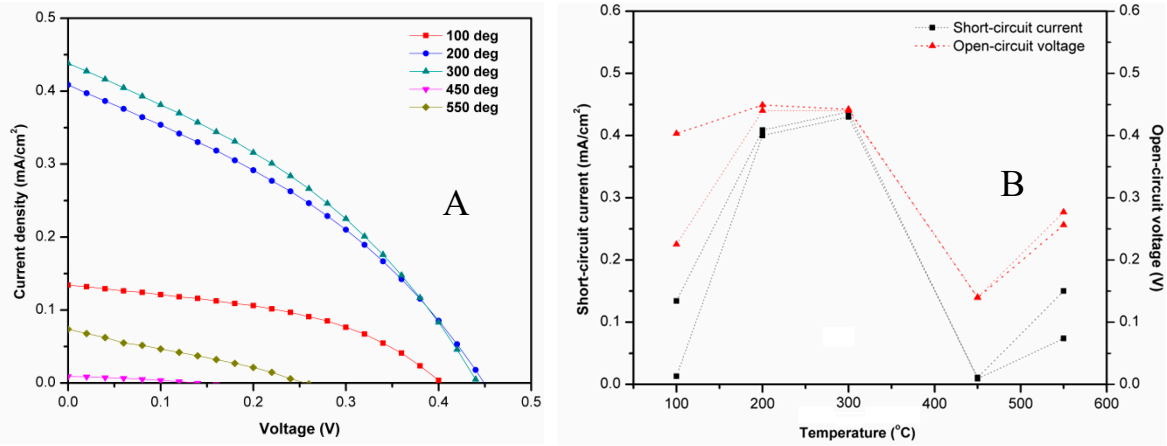

Figure 6. Current-voltage curve of annealed BiOI at different temperatures (**A**) and short-circuit current and open-circuit voltage as the function of temperature (**B**).

Table 1. Photovoltaic cell parameter of annealed BiOI at different temperatures. J_{sc}: short-circuit current; V_{oc}: open circuit voltage; R_{sh}: shunt resistance; R_s: series resistance.

Temperature (°C)	J_{sc} (mA/cm^2)	V_{oc} (V)	Fill Factor	Efficiency (%)	R_{sh} ($10^3 \times \Omega$ cm^2)	R_s ($10^3 \times \Omega$ cm^2)
100	0.133	0.403	0.440	0.023	9.183	0.170
200	0.408	0.449	0.349	0.064	11.49	0.156
300	0.438	0.442	0.357	0.069	10.82	0.148
450	0.009	0.139	0.320	0.0004	7.898	0.162
550	0.073	0.256	0.276	0.0052	9.247	0.112

We observed that annealed material at 300 °C showed the best performance in comparison to the others. It was 0.438 mA/cm^2, which was almost four times higher than the resulted at 100 °C. In general, the photovoltaic properties of an electrochemical cell using porous material are affected by particle size, conductivity, lifetime, crystal orientation, etc. SEM images (Figure 3) and XRD patterns (Figure 1) show that the size of (001) nanosheets becomes larger and the FWHM of peaks becomes broader with increasing the annealing temperature from 100 °C to 300 °C, which suggests that the larger particle sizes with high conductivities were obtained at 300 °C annealing, which is suitable for electrochemical devices. The sample at 300 °C may also have had the bigger surface area for better contact with liquid electrolyte material. This phenomenon is likely to happen in the TiO_2 porous-based solar cell. As a result, $Bi_7O_9I_3$ could perform good interaction between the semiconductor material and iodine electrolyte in the photovoltaic device for exhibiting a higher J_{sc} value. The contact angle check also revealed the increase of wettability due to the annealing treatment on BiOI from 100 °C to 300 °C (Figure 7). A declining contact angle occurred after the annealing treatment was set up to 300 °C. This indicated that $Bi_7O_9I_3$ had better contact with water than BiOI. As a consequence, the polar organic solvent, which is commonly used in the electrolyte liquid for dye-sensitized solar cells (DSSC), had more preference to make a good interaction with the more polar film surface. This trend was also matched to the previous report in BiOI solar cell [50]. Though overall J_{sc} values in this report were lower than the reported BiOI solar cell [51] due to its bulky structure, it is interesting to note that $Bi_7O_9I_3$ had the better photovoltaic activity in comparison to its parent BiOI. This model is similar to the photocatalytic behavior of $Bi_7O_9I_3$ [1,26,29].

Figure 7. The contact angle of annealed BiOI at different temperatures (**A**–**C**): 100 °C, 300 °C, and 550 °C.

Normally, due to the increase in bandgap energy, the V_{oc} also improves since the thermodynamically open-circuit voltage limit is determined from the bandgap energy of materials. However, the annealing treatment resulted in a lower V_{oc} value. A plummet drop of Voc existed for the annealed sample at 450 °C, which might have been influenced by shunt resistance (R_{sh}). The small R_{sh} value caused the low V_{oc} in the photovoltaic device. Thus, the performance parameter in the photovoltaic device decreased. On the contrary, the higher R_{sh} value had an impact on the Voc enhancement, and the higher R_s will cause the lowering of the J_{sc} value. The changing in shunt resistance produced another current way in a photovoltaic cell, which could have reduced its current flow and voltage. Therefore, the changing in its bandgap energy and a slight increase of its R_{sh} value in comparison to others may have been responsible for the higher V_{oc} of annealed BiOI at 300 °C. The illustrated band structure of annealed BiOI is sketched in Figure 5B.

Through this work, we expect that if a better quality of BiOI (coming from its morphology and material size) is used, cell performance will tend to be higher than our results. It has been reported that a single BiOI solar cell could reach a J_{sc} value up to 2 mA/cm^2 [51]. Therefore, by using suitable electrons and holes transport materials, it can be suggested to apply the bismuth oxyiodides and its derivations, like $Bi_7O_9I_3$, for the absorber in the reported device structure [11].

4. Conclusions

In our work, the synthesis and annealing treatment of BiOI, as well as its effect on photovoltaic activity, were studied. We highlighted that the annealing treatment of BiOI resulted in oxygen-abundant and iodine-deficient bismuth materials from the parent BiOI. The changing in temperature affected the structural, morphological, and its optical properties of BiOI films. As a consequence, it performed different parameters of the photovoltaic cell. The annealed BiOI at 300 °C, 450 °C, and 550 °C allowed for the transformation from BiOI to $Bi_7O_9I_3$, Bi_5O_7I, and β-Bi_2O_3. The heated material at 300 °C, as $Bi_7O_9I_3$ had the best photovoltaic cell performance in comparison to other materials—its efficiency was three times higher than that of BiOI. The broadening on the FWHM of (001) as the effect of annealing treatment, the different grain size of this material, and an adequate harvesting light ability can be expected as the reasons why $Bi_7O_9I_3$ is more suitable in photovoltaic applications than BiOI. This behavior is in line with the performance of $Bi_7O_9I_3$ in reported photocatalytic reaction works. Based on this result, $Bi_7O_9I_3$ can be suggested to be implemented as the absorber in photovoltaic devices involving matched hole and electron transport layers.

Author Contributions: Conceptualization, A.A.P. and T.S.; methodology, A.A.P. and S.K.; validation, S.K., N.K. and T.S.; formal analysis, A.A.P.; investigation, A.A.P.; resources, T.S.; writing—original draft preparation, A.A.P.; writing—review and editing, S.K., N.K. and T.S.; supervision, S.K., N.K. and T.S.

Funding: This research received no external funding.

Acknowledgments: A.A.P. would like to thank the financial support from MORA Scholarship, Ministry of Religious Affairs, The Republic of Indonesia for the Ph.D. scholarship (No. 36/Dt.I.IV/4/PP.07/01/2017).

Conflicts of Interest: The authors declare no conflict of interest. The funders had no role in the design of the study; in the collection, analyses, or interpretation of data; in the writing of the manuscript, or in the decision to publish the results.

References

1. Lee, W.W.; Lu, C.S.; Chuang, C.W.; Chen, Y.J.; Fu, J.Y.; Siao, C.W.; Chen, C.C. Synthesis of bismuth oxyiodides and their composites: Characterization, photocatalytic activity, and degradation mechanisms. *RSC Adv.* **2015**, *5*, 23450–23463. [CrossRef]
2. He, R.; Zhang, J.; Yu, J.; Cao, S. Room-temperature synthesis of BiOI with tailorable (001) facets and enhanced photocatalytic activity. *J. Colloid Interface Sci.* **2016**, *478*, 201–208. [CrossRef]
3. Zhang, X.; Zhang, L. Electronic and band structure tuning of ternary semiconductor photocatalysts by self doping: The case of BiOI. *J. Phys. Chem. C* **2010**, *114*, 18198–18206. [CrossRef]
4. Niu, J.; Dai, P.; Zhang, Q.; Yao, B.; Yu, X. Microwave-assisted solvothermal synthesis of novel hierarchical BiOI/rGO composites for efficient photocatalytic degardation of organic pollutants. *Appl. Surf. Sci.* **2018**, *430*, 165–175. [CrossRef]
5. Zhang, X.; Zhang, L.; Xie, T.; Wang, D. Low-temperature synthesis and high visible-light-induced photocatalytic activity of BiOI/TiO_2 heterostructures. *J. Phys. Chem. C* **2009**, *113*, 7371–7378. [CrossRef]
6. Cao, J.; Xu, B.; Luo, B.; Lin, H.; Chen, S. Novel BiOI/BiOBr heterojunction photocatalysts with enhanced visible light photocatalytic properties. *Catal. Commun.* **2011**, *13*, 63–68. [CrossRef]
7. Hou, J.; Jiang, K.; Shen, M.; Wei, R.; Wu, X.; Idrees, F.; Cao, C. Micro and nano hierachical structures of BiOI/activated carbon for efficient visible-light-photocatalytic reactions. *Sci. Rep.* **2017**, *7*, 11665. [CrossRef]
8. Hao, R.; Xiao, X.; Zuo, X.; Nan, J.; Zhang, W. Efficient adsorption and visible-light photocatalytic degradation of tetracycline hydrochloride using mesoporous BiOI microspheres. *J. Hazard. Mater.* **2012**, *209*, 137–145. [CrossRef]
9. Cheng, H.; Huang, B.; Dai, Y.; Qin, X.; Zhang, X. One-Step Synthesis of the Nanostructured AgI/BiOI Composites with Highly Enhanced Visible-Light Photocatalytic Performances. *Langmuir* **2010**, *26*, 6618–6624. [CrossRef]
10. Han, A.; Zhang, H.; Chuah, G.K.; Jaenicke, S. Influence of the halide and exposed facets on the visible-light photoactivity of bismuth oxyhalides for selective aerobic oxidation of primary amines. *Appl. Catal. B Environ.* **2017**, *219*, 269–275. [CrossRef]
11. RHoye, L.Z.; Lee, L.C.; Kurchin, R.C.; Huq, T.N.; Zhang, K.H.L.; Sponseller, M.; Nienhaus, L.; Brandt, R.E.; Jean, J.; Polizzotti, J.A.; et al. Strongly Enhanced Photovoltaic Performance and Defect Physics of Air-Stable Bismuth Oxyiodide (BiOI). *Adv. Mater.* **2017**, *29*, 1–10.
12. Wang, L.; Daoud, W.A. BiOI/TiO_2-nanorod array heterojunction solar cell: Growth, charge transport kinetics and photoelectrochemical properties. *Appl. Surf. Sci.* **2015**, *324*, 532–537. [CrossRef]
13. Sfaelou, S.; Raptis, D.; Dracopoulos, V.; Lianos, P. BiOI solar cells. *RSC Adv.* **2015**, *5*, 95813–95816. [CrossRef]
14. Zhang, Y.; Pei, Q.; Liang, J.; Feng, T.; Zhou, X.; Mao, H.; Zhang, W.; Hisaeda, Y.; Song, X.M. Mesoporous TiO_2-Based Photoanode Sensitized by BiOI and Investigation of Its Photovoltaic Behavior. *Langmuir* **2015**, *31*, 10279–10284. [CrossRef]
15. Wang, K.; Jia, F.; Zhang, L. Facile construction of low-cost flexible solar cells with p-type BiOI nanoflake arrays fabricated via oriented attachment. *Mater. Lett.* **2013**, *92*, 354–357. [CrossRef]
16. Wang, K.; Jia, F.; Zheng, Z.; Zhang, L. Crossed BiOI flake array solar cells. *Electrochem. Commun.* **2010**, *12*, 1764–1767. [CrossRef]
17. Zhang, Y.; Li, Y.; Sun, W.; Yuan, C.; Wang, B.; Zhang, W.; Song, X.M. Fe_2O_3/BiOI-Based Photoanode with n-p Heterogeneous Structure for Photoelectric Conversion. *Langmuir* **2017**, *33*, 12065–12071. [CrossRef]
18. Lei, Y.; Wang, G.; Song, S.; Fan, W.; Pang, M.; Tang, J.; Zhang, H. Room temperature, template-free synthesis of BiOI hierarchical structures: Visible-light photocatalytic and electrochemical hydrogen storage properties. *Dalt. Trans.* **2010**, *39*, 3273–3278. [CrossRef]
19. Xiao, X.; Zhang, W.D. Facile synthesis of nanostructured BiOI microspheres with high visible light-induced photocatalytic activity. *J. Mater. Chem.* **2010**, *20*, 5866–5870. [CrossRef]
20. Long, Y.; Han, Q.; Yang, Z.; Ai, Y.; Sun, S.; Wang, Y.; Liang, Q.; Ding, M. A novel solvent-free strategy for the synthesis of bismuth oxyhalides. *J. Mater. Chem. A* **2018**, *6*, 13005–13011. [CrossRef]
21. Meledandri, C.J.; Stolarczyk, J.K.; Ghosh, S.; Brougham, D.F. Nonaqueous Magnetic Nanoparticle Suspensions with Controlled Particle Size and Nuclear Magnetic Resonance Properties. *Langmuir* **2008**, *24*, 14159–14165. [CrossRef]

22. Demortière, A.; Panissod, P.; Pichon, B.P.; Pourroy, G.; Guillon, D.; Donnio, B.; Bégin-Colin, S. Size-dependent properties of magnetic iron oxidenanocrystals. *Nanoscale* **2011**, *3*, 225–232.
23. Effenberger, F.B.; Couto, R.A.; Kiyohara, P.K.; Machado, G.; Masunaga, S.H.; Jardim, R.F.; Rossi, L.M. Economically attractive route for the preparation of high quality magnetic nanoparticles by the thermal decomposition of iron(III) acetylacetonate. *Nanotechnology* **2017**, *28*, 115603. [CrossRef]
24. Hufschmid, R.; Arami, H.; Ferguson, R.M.; Gonzales, M.; Teeman, E.; Brush, L.N.; Browning, N.D.; Krishnan, K.M. Synthesis of phase-pure and monodisperse iron oxide nanoparticles by thermal decomposition. *Nanoscale* **2015**, *7*, 11142–11154. [CrossRef]
25. Baaziz, W.; Pichon, B.P.; Fleutot, S.; Liu, Y.; Lefevre, C.; Greneche, J.M.; Toumi, M.; Mhiri, T. Begin-Colin, Magnetic Iron Oxide Nanoparticles: Reproducible Tuning of the Size and Nanosized-Dependent Composition, Defects, and Spin Canting. *J. Phys. Chem. C* **2014**, *118*, 3795–3810. [CrossRef]
26. Long, M.; Hu, P.; Wu, H.; Chen, Y.; Tan, B.; Cai, W. Understanding the composition and electronic structure dependent photocatalytic performance of bismuth oxyiodides. *J. Mater. Chem. A* **2015**, *3*, 5592–5598. [CrossRef]
27. Xiao, X.; Liu, C.; Hu, R.; Zuo, X.; Nan, J.; Li, L.; Wang, L. Oxygen-rich bismuth oxyhalides: Generalized one-pot synthesis, band structures and visible-light photocatalytic properties. *J. Mater. Chem.* **2012**, *22*, 22840. [CrossRef]
28. Xia, J.; Ji, M.; Di, J.; Wang, B.; Yin, S.; He, M.; Zhang, Q.; Li, H. Improved photocatalytic activity of few-layer $Bi_4O_5I_2$ nanosheets induced by efficient charge separation and lower valence position. *J. Alloy. Compd.* **2017**, *695*, 922–930. [CrossRef]
29. Xiao, X.; Zhang, W.D. Hierarchical $Bi_7O_9I_3$ micro/nano-architecture: Facile synthesis, growth mechanism, and high visible light photocatalytic performance. *RSC Adv.* **2011**, *1*, 1099–1105. [CrossRef]
30. Yang, J.; Xu, L.; Liu, C.; Xie, T. Preparation and photocatalytic activity of porous Bi_5O_7I nanosheets. *Appl. Surf. Sci.* **2014**, *319*, 265–271. [CrossRef]
31. Cheng, H.; Huang, B.; Lu, J.; Wang, Z.; Xu, B.; Qin, X.; Zhang, X.; Dai, Y. Synergistic effect of crystal and electronic structures on the visible-light-driven photocatalytic performances of Bi_2O_3 polymorphs. *Phys. Chem. Chem. Phys.* **2010**, *12*, 15468–15475. [CrossRef]
32. Zhang, D.; Wang, F.; Cao, S.; Duan, X. Investigation on enhanced photocatalytic degradation of bisphenol A with bismuth oxyiodide catalyst using response surface methodology. *RSC Adv.* **2018**, *8*, 5967–5975. [CrossRef]
33. Ren, X.; Yao, J.; Cai, L.; Li, J.; Cao, X.; Zhang, Y.; Wang, B.; Wei, Y. Band gap engineering of BiOI via oxygen vacancies induced by graphene for improved photocatalysis. *New J. Chem.* **2019**, *43*, 1523–1530. [CrossRef]
34. Chou, S.Y.; Chen, C.C.; Dai, Y.M.; Lin, J.H.; Lee, W.W. Novel synthesis of bismuth oxyiodide/graphitic carbon nitride nanocomposites with enhanced visible-light photocatalytic activity. *RSC Adv.* **2016**, *6*, 33478–33491. [CrossRef]
35. Khedreteralid, M.; Mujahid, M.; Amin, S.; Rawat, R.S.; Nusair, A.; Deen, G.R. Effect of surfactant and heat treatment on morphology, surface area and crystallinity in hydroxyapatite nanocrystals. *Ceram. Int.* **2013**, *39*, 39–50.
36. Yang, J.; Xie, T.; Liu, C.; Xu, L. Facile Fabrication of Dumbbell-Like β-Bi_2O_3/Graphene Nanocomposites and Their Highly Efficient Photocatalytic Activity. *Materials* **2018**, *11*, 1359. [CrossRef]
37. Wang, H.; Xu, L.; Liu, C.; Lu, Y.; Feng, Q.; Wu, T.; Wang, R. Composite Magnetic Photocatalyst $Bi_5O_7I/Mn_xZn_{1-x}Fe_2O_4$: Hydrothermal-Roasting Preparation and Excellent Photocatalytic Activity. *Nanomaterials* **2019**, *9*, 118. [CrossRef]
38. Park, Y.; Na, Y.; Pradhan, D.; Min, B.K.; Sohn, Y. Adsorption and UV/Visible photocatalytic performance of BiOI for methyl orange, Rhodamine B and methylene blue: Ag and Ti-loading effects. *CrystEngComm* **2014**, *16*, 3155–3167. [CrossRef]
39. Fang, M.; Jia, H.; He, W.; Lei, Y.; Zhang, L.; Zheng, Z. Construction of flexible photoelectrochemical solar cells based on ordered nanostructural BiOI/Bi_2S_3 heterojunction films. *Phys. Chem. Chem. Phys.* **2015**, *17*, 13531–13538. [CrossRef]
40. Liu, C.; Wang, X.J. Room temperature synthesis of $Bi_4O_5I_2$ and Bi_5O_7I ultrathin nanosheets with a high visible light photocatalytic performance. *Dalt. Trans.* **2016**, *45*, 7720–7727. [CrossRef]

41. Díaz-Guerra, C.; Almodóvar, P.; Camacho-López, M.; Camacho-López, S.; Piqueras, J. Formation of β-Bi_2O_3 and δ-Bi_2O_3 during laser irradiation of Bi films studied in-situ by spatially resolved Raman spectroscopy. *J. Alloy. Compd.* **2017**, *723*, 520–526.
42. Lu, J.; Wu, J.; Xu, W.; Cheng, H.; Qi, X.; Li, Q.; Zhang, Y.; Guan, Y.; Ling, Y.; Zhang, Z. Room temperature synthesis of tetragonal BiOI photocatalyst with surface heterojunction between (0 0 1) facets and (1 1 0) facets. *Mater. Lett.* **2018**, *219*, 260–264. [CrossRef]
43. Du, Y.; Huang, R.; Song, R.; Ma, L.B.; Liu, C.; Li, C.R.; Cao, Z.X. Effect of oxygen inclusion on microstructure and thermal stability of copper nitride thin films. *J. Mater. Res.* **2007**, *22*, 3052–3057. [CrossRef]
44. Brugnoli, E.; Björkman, O. Chloroplast movements in leaves: Influence on chlorophyll fluorescence and measurements of light-induced absorbance changes related to ΔpH and zeaxanthin formation. *Photosynth. Res.* **1992**, *32*, 23–35. [CrossRef]
45. Ma, F.Q.; Yao, J.W.; Zhang, Y.F.; Wei, Y. Unique band structure enhanced visible light photocatalytic activity of phosphorus-doped BiOI hierarchical microspheres. *RSC Adv.* **2017**, *7*, 36288–36296. [CrossRef]
46. Sun, S.; Wang, W.; Zhang, L.; Zhou, L.; Yin, W.; Shang, M. Visible light-induced efficient contaminant removal by Bi_5O_7I. *Environ. Sci. Technol.* **2009**, *43*, 2005–2010. [CrossRef]
47. Schlesinger, M.; Weber, M.; Schulze, S.; Hietschold, M.; Mehring, M. Metastable β-Bi_2O_3 Nanoparticles with Potential for Photocatalytic Water Purification Using Visible Light Irradiation. *ChemistryOpen* **2013**, *2*, 146–155. [CrossRef]
48. Huang, Y.; Li, H.; Balogun, M.S.; Liu, W.; Tong, Y.; Lu, X.; Ji, H. Oxygen Vacancy Induced Bismuth Oxyiodide with Remarkably Increased Visible-Light Absorption and Superior Photocatalytic Performance. *ACS Appl. Mater. Interfaces* **2014**, *6*, 22920–22927. [CrossRef]
49. Wang, Z.S.; Cui, Y.; Hara, K.; Dan-oh, Y.; Kasada, C.; Shinpo, A. Shinpo, A High-Light-Harvesting-Efficiency Coumarin Dye for Stable Dye-Sensitized Solar Cells. *Adv. Mater.* **2007**, *19*, 1138–1141. [CrossRef]
50. Putri, A.A.; Kato, S.; Kishi, N.; Soga, T. Angle dependence of synthesized BiOI prepared by dip coating and its effect on the photovoltaic performance. *Jpn. J. Appl. Phys.* **2019**, *58*, SAAD09. [CrossRef]
51. Putri, A.A.; Kato, S.; Kishi, N.; Soga, T. Relevance of precursor molarity in the prepared bismuth oxyiodide films by successive ionic layer adsorption and reaction for solar cell application. *J. Sci. Adv. Mater. Devices* **2019**, *4*, 116–124. [CrossRef]